Neighbor-specific gene expression revealed from physically interacting cells during mouse embryonic development

Junil Kim[a,b,1] (ORCID), Michaela Mrugala Rothová[c,1], Esha Madan[d,1], Siyeon Rhee[e], Guangzheng Weng[a], António M. Palma[d] (ORCID), Linbu Liao[a] (ORCID), Eyal David[f], Ido Amit[f], Morteza Chalabi Hajkarim[a], Vignesh Vudatha[g] (ORCID), Andrés Gutiérrez-García[d], Eduardo Moreno[d], Robert Winn[h], Jose Trevino[g], Paul B. Fisher[h,i,j] (ORCID), Joshua M. Brickman[c,2] (ORCID), Rajan Gogna[h,i,j,2], and Kyoung Jae Won[a,k,2]

Development of multicellular organisms is orchestrated by persistent cell–cell communication between neighboring partners. Direct interaction between different cell types can induce molecular signals that dictate lineage specification and cell fate decisions. Current single-cell RNA-seq technology cannot adequately analyze cell–cell contact-dependent gene expression, mainly due to the loss of spatial information. To overcome this obstacle and resolve cell–cell contact-specific gene expression during embryogenesis, we performed RNA sequencing of physically interacting cells (PIC-seq) and assessed them alongside similar single-cell transcriptomes derived from developing mouse embryos between embryonic day (E) 7.5 and E9.5. Analysis of the PIC-seq data identified gene expression signatures that were dependent on the presence of specific neighboring cell types. Our computational predictions, validated experimentally, demonstrated that neural progenitor (NP) cells upregulate *Lhx5* and *Nkx2-1* genes, when exclusively interacting with definitive endoderm (DE) cells. Moreover, there was a reciprocal impact on the transcriptome of DE cells, as they tend to upregulate *Rax* and *Gsc* when in contact with NP cells. Using individual cell transcriptome data, we formulated a means of computationally predicting the impact of one cell type on the transcriptome of its neighboring cell types. We have further developed a distinctive spatial-t-distributed stochastic neighboring embedding to display the pseudospatial distribution of cells in a 2-dimensional space. In summary, we describe an innovative approach to study contact-specific gene regulation during embryogenesis.

single-cell RNA sequencing | PIC-seq | contact-specific expression | mouse embryonic development | spatial-tSNE

Cell–cell contact is important for cell-fate specification during development (1–9). Cell–cell communication including direct cell–cell contact directs embryonic patterning, cell type specification, and organ formation (6). Removing specific tissue or placing ectopic explants into various embryonic regions can dynamically change the fate of cells adjacent to the manipulated area (3). For instance, manipulation with the crucial signaling center, anterior visceral endoderm, causes defects in the specification of forebrain identity later in development (10). It is well-recognized that ectopic grafts of signaling centers such as the node (N) or Spemann organizer can induce a secondary neural axis (11, 12). Even with the importance of various cell type interactions for development, it is still challenging to study gene expression changes in association with neighboring tissue. While the grafting experiments have significantly enhanced our understanding of the inductive ability of various neighboring cell types (11), these experiments are technically demanding and/or are not always feasible.

Single-cell transcriptional profiling has been successfully applied to identify cell types and their developmental trajectory during mouse organogenesis (13–15). However, the loss of spatial information in single-cell RNA sequencing (scRNA-seq) makes it difficult to trace the genes induced and regulated by the interaction of different cell types. Coexpression of ligand–receptor pairs from scRNA-seq data has been used to predict interacting cell types (16, 17). However, there are other modes of cell communication besides ligand–receptor, such as direct cell communication through gap junctions (18). It is still difficult to accurately detect neighboring tissue-specific gene expression changes.

Recently, RNA sequencing of multiple-interacting cells has been used to measure the transcriptome of physically interacting cells (PICs) without relying on ligand–receptor coexpression (19–23). ProximID identified the interacting cell types in the bone marrow and the small intestine in mice using the transcriptome of two or more PICs by applying mild dissociation of cells (19). Sequencing of physically interacting cells (PIC-seq) was employed to interrogate interactions of immune and epithelial cells in neonatal murine lungs (22) and to understand transcriptomic changes of liver endothelial cells across liver

Significance

Physical contact between neighboring cells is known to induce transcriptional changes in the interacting partners. Accurate measurement of these cell–cell contact-based influences on the transcriptome is a very difficult experimental task. However, determining such transcriptional changes will highly enhance our understanding for the developmental processes. Current scRNA-seq technology isolates the tissue into individual cells, making it hard to determine the potential transcriptomic changes due to cell-cell interactions. Here, we combined PIC-seq and computational algorithms to identify cell type contact-dependent transcriptional profiles focusing on endoderm development. We have computationally identified and experimentally validated specific gene expression patterns depending on the presence of specific neighboring cell types. Our study suggests a new approach to disentangle the role of cell–cell interactions during embryogenesis.

[1]J.K., M.M.R., and E.M. contributed equally to this work.

[2]To whom correspondence may be addressed. Email: joshua.brickman@sund.ku.dk, rajangogna@gmail.com, or kyoungjae.won@cshs.org.

zones (20). Cell–cell interactions by multiple sequencing were applied to identify interacting cell types in the gut epithelium, lung, and spleen (23).

While previous approaches using multiple interacting cells have mainly focused on investigating interacting cell types, we hypothesize that interacting multi cells will retain gene expression derived from the physical interaction defined by these disparate cell types. To identify cell type contact-associated transcriptional profiles focusing on endoderm development, we dissected the developing mouse embryos (at E7.5, E8.5, and E9.5), sorted FOXA2^{Venus} expressing cells, and used this material for PIC-seq. Using PIC-seq, we captured both homotypic and heterotypic cell clusters physically interacting with each other. Interestingly, we identified various sets of genes expressed in the heterotypic PICs but not each individual cell type. Computational analysis identified the cell types expressing unique gene sets specific to their neighbors. For instance, *Lhx5* and *Nkx2-1* were expressed exclusively in the neural progenitor (NP) cells that physically interact with definitive endoderm (DE) cells and *Gsc* and *Rax* were expressed in the DE cells interacting with NP cells. Some of these neighboring cell-type-specific genes were associated with the development of specific embryonic regions. Validation using Geo-seq (24) which provides transcriptome from the dissected developing mouse embryos

confirmed that we had successfully identified spatially organized sets of cells and neighboring cell-specific genes. Additionally, we designed experimental tools to investigate and successfully validate the computational predictions. Notably, we were able to predict neighboring cell types from scRNA-seq based on the cell contact-specific genes. We further emulated the anatomy of the mouse embryos by visualizing cell–cell contact information and neighboring cell-specific gene expression in a modified t-distributed stochastic neighbor embedding plot spatial-t-distributed stochastic neighboring embedding (spatial-tSNE). Our results suggest that the local environment information retained in the transcriptome of individual cells can be used to reconstruct potential spatial gene regulation patterns during development.

Results

Mapping of PIC-seq Data onto Cell Types in the Mouse Embryo.
To identify transcriptional profiles influenced by cell–cell contact during development with focus on the endoderm, we took advantage of a mouse line in which a Venus fluorescent protein had been fused to the endoderm regulator FOXA2 (25) to identify FOXA2-expressing endoderm cells from embryos ranging from E7.5 to E9.5 (Fig. 1*A*). We obtained PIC-seq after mild
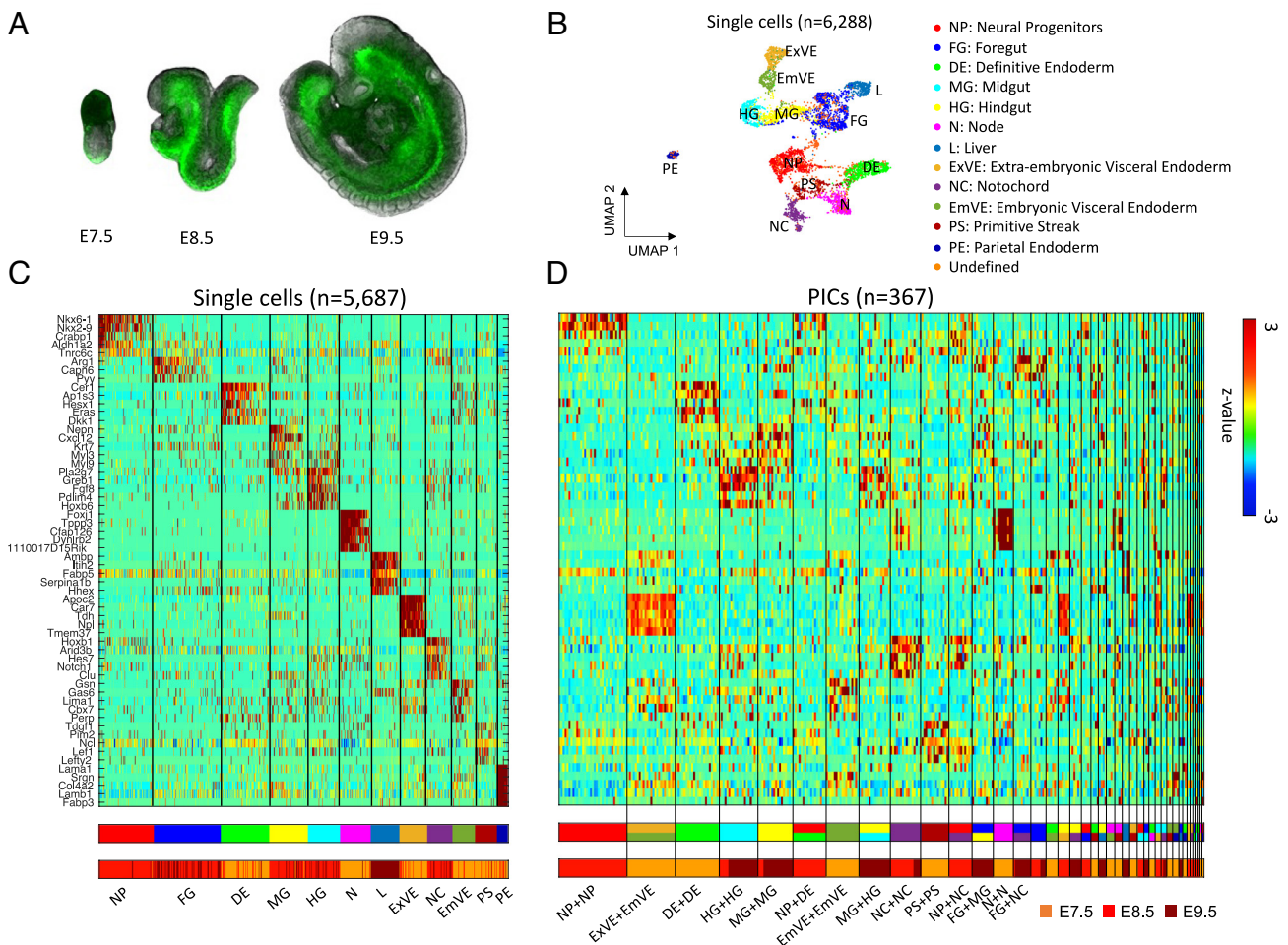
Fig. 1. PIC-seq for developing mouse embryos. (*A*) A cartoon of mouse embryos (E7.5, E8.5, and E9.5) with fluorescently tagged FOXA2^{Venus} based on the embryo images in ref. (26). (*B*) Clustering analysis identifies 12 cell types from scRNA-seq data from the developing mouse embryos. (*C*) A heatmap of the marker genes exhibits distinct expression profiles for the 12 identified cell types. The cell types from the clustering analysis and the embryonic days are shown at the *Bottom*. (*D*) Gene expression profiles of the identified marker genes for 367 PICs. The predicted cell types for the PICs are shown and their embryonic days are shown at the *Bottom*.

dissociation of these mouse embryos followed by fluorescence-activated cell sorting (FACS) against FOXA2^{Venus}, and cell size was used to filter out potential single cells.

After applying stringent quality control measures, RNA sequencing data from 367 PICs were obtained using massively parallel RNA single-cell sequencing (MARS-seq) technology (27, 28). To analyze the PIC-seq data, we used scRNA-seq from MARS-seq (total of 6,288 cells) against mouse embryos obtained at matching time points (26). Data are presented to summarize the number of PIC-seq pairs and the number of cells from scRNA-seq obtained at each stage as well as the gene and read count distribution (*SI Appendix*, Fig. S1).

From the scRNA-seq, we identified 13 clusters: neural progenitors (NP; n = 767), foregut (FG; n = 927), midgut (MG; n = 537), hindgut (HG; n = 444), definitive endoderm (DE; n = 677), liver (L; n = 402), extra-embryonic visceral endoderm (ExVE; n = 385), embryonic visceral endoderm (EmVE; n = 314), primitive streak (PS; n = 302), (N; n = 422), notochord (NC; n = 350), parietal endoderm (PE; n = 160), and one undefined cluster (Fig. 1 *B* and *C*) and (*SI Appendix*, Fig. S2). From the cluster analysis, we identified 545 cell-type-specific marker genes (false discovery rate (FDR) < 0.01 and log ratio > 0.4) (Dataset S1).

To annotate the cell types of the PICs, we used the cell type marker genes identified from scRNA-seq clustering (Fig. 1*C*). For this purpose, multiclass support vector machines (SVMs) were trained with artificial doublets from two randomly selected single cells for the three time points. SVMs were known to perform well for classifying high-dimensional data even with a small number of samples (29). The trained SVMs classified the 367 PICs into homotypic and heterotypic combinations of cell types (Fig. 1*D* and Dataset S2). The error rate of 10-fold cross-validation for the SVMs were 17.27%, 18.76%, and 28.56% in E7.5, E8.5, and E9.5, respectively, suggesting comparable performance with a previous

deconvolution approach (22). The designated marker genes were well expressed in the annotated PICs (Fig. 1*D*). Notably, the frequencies of the heterotypic combinations identified using PICs were significantly high as compared with the combination of erroneous doublets identified using DoubletFinder (30) (*SI Appendix*, Fig. S3). The observed heterotypic combinations such as ExVE+EmVE (at E7.5) and NP+DE (at E8.5) reflect the neighboring tissues in developing mouse embryos (13, 31, 32).

PIC-seq Enables Detection of Cell–Cell Contact-Specific Gene Expression. To examine cell–cell contact-specific gene expression, we investigated genes highly expressed in the heterotypic PICs but not in the homotypic combinations of each individual cell type. For the PIC types with at least 10 cell type pairs (ExVE+EmVE in E7.5, NP+DE in E8.5, NP+NC in E8.5, MG+HG in E9.5, and FG+MG in E9.5), we investigated neighboring cell–cell contact-associated gene expression (Fig. 2 and *SI Appendix*, Figs. S4–S7). We identified 167 genes highly expressed in the heterotypic PICs as compared to the expected expression levels for individual cell types obtained from scRNA-seq (FDR < 0.01 & log ratio > 0.5) (Dataset S3). For instance, the heterotypic PICs for NP+DE expressed genes such as *Lhx5*, *Nkx2-1*, and *Gsc*. These PICs also expressed the marker genes for NP and DE: *Crabp1* and *Col8a1* for NP and *Trh* and *Slc2a3* for DE (Fig. 2 *A* and *B*). Interestingly, some of the identified neighboring cell-type-specific genes are known to play crucial roles during development. *Lhx5* is known to promote forebrain development (33). *Nkx2-1* is required for the proper specification of interneuron subtypes (34). *Gsc* is a known marker of the anterior endoderm (EA) (35) and prechordal plate (36) and has been implicated in embryonic stem cells (ESC) differentiation to DE differentiation (37–39).

The 54 genes highly expressed in the heterogeneous PIC of NP+DE at E8.5 were linked to endodermal or neuroectodermal
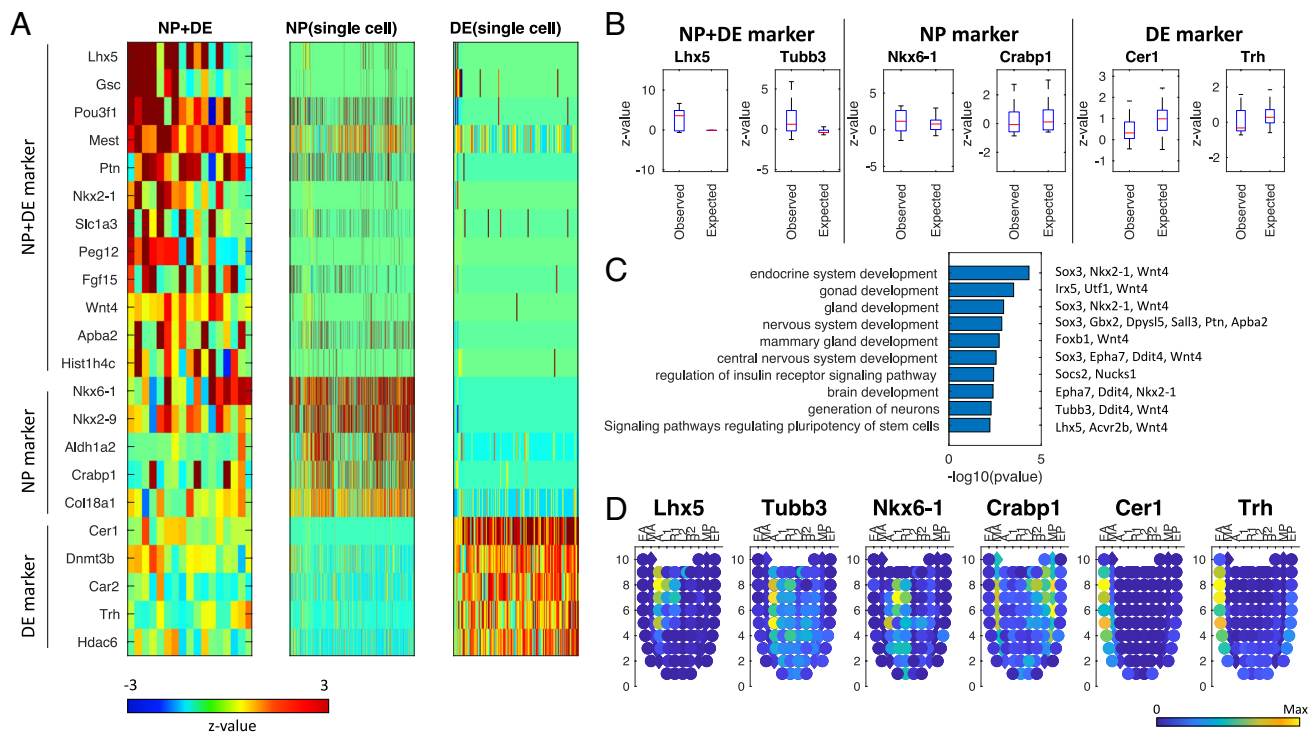
Fig. 2. PIC-seq analysis identified genes highly expressed in NP+DE. (*A*) A heatmap of PIC-seq of NP+DE showed contact-specific expression as well as the marker genes for NP and DE. (*B*) Contact-specific expression levels are significantly high for the PIC-seq compared with the expected expression levels obtained from scRNA-seq. (*C*) GO and KEGG pathway terms enriched in the contact-specific genes. (*D*) Validation of the contact-specific marker genes using Geo-seq data. EA: anterior endoderm; MA: anterior mesoderm; A: anterior; L1: anterior left lateral; R1: anterior right lateral; L2: posterior left lateral; R2: posterior right lateral; P: posterior; MP: posterior mesoderm; EP: posterior endoderm.

embryo development including gland development (*Sox3*, *Nkx2-1*, and *Wnt4*, *P* value: 1.1E-3) and nervous system development (*Sox3*, *Gbx2*, *Dpysl5*, *Sall3*, *Ptn*, and *Apba2*, *P* value: 1.38E–3) based on the gene ontology (GO) terms and Kyoto Encyclopedia of Genes and Genomes (KEGG) pathways enrichment tests (40) (Fig. 2*C*). The 39 NP+NC contact-specific genes were mainly associated with mesodermal development, e.g., *Mesp1*, *Meox1*, *Lef1* (*SI Appendix,* Fig. S6). Our results suggest that PIC-seq could be used to identify and stratify genes induced in regions where different cell types are in physical contact during embryonic differentiation.

In the same manner, we identified 50 genes lowly expressed in the heterotypic PICs as compared to the expected expression levels for individual cell types obtained from scRNA-seq (FDR < 0.01 and log ratio > 0.5) (Dataset S4 and *SI Appendix,* Fig. S8). Among the 12 genes downregulated in the heterogenous PIC of NP+DE, we found *Sox17*, an important factor for cardiac mesoderm specification (41). Among the 27 downregulated genes in the heterogenous PIC of ExVE+EmVE is *Ctsh*, an important factor for lung morphogenesis (42).

Contact-Specific Gene Expression Is Spatially Localized at the Boundary Regions between Two Cell Types. To validate the spatial expression of contact-specific marker genes, we used a publicly available Geo-seq dataset (24) which contains transcriptome from 83 dissected regions in the developing mouse embryos at E7.5 (*SI Appendix,* Figs. S9–S11). DE marker genes (*Cer1* and *Trh*) were strongly expressed in the EA, while NP marker genes (*Nkx6-1,* and *Crabp1*) were strongly expressed interior to the endoderm in Geo-seq (Fig. 2*D* and *SI Appendix,* Fig. S9). Intriguingly, the contact-specific genes (*Lhx5* and *Tubb3*) were expressed in-between the regions expressing NP- and DE-specific genes (Fig. 2*D* and *SI Appendix,* Fig. S10). The averaged profiles for NP+DE genes also showed the strongest expression of the contact-specific genes in between NP- and DE-marked regions in the Geo-seq (*SI Appendix,* Fig. S11*A*).

In addition, we found that the ExVE+EmVE-specific genes were mainly expressed in-between the regions marked by the two cell types (upper part of the corn plot) in the Geo-seq dataset (*SI Appendix,* Fig. S11*B*). While the nature of the Geo-seq dataset is such that it does not include structures like gut or NC, we identify coexpression of contact-associated genes, e.g., the NP+NC-specific genes were highly expressed in the posterior mesoderm (*SI Appendix,* Fig. S11*C*), which was located between the posterior ectoderm and N region (bottom of the corn plot). Our results indicate that the contact-specific genes obtained from PIC-seq reflect the original and accurate spatial expression.

To further confirm our observations, we used the public seqFISH data (43) from mouse embryos at E8.5–E8.75 for 351 genes. The cell type annotation (brain/spinal cord, gut tube, and DE) visualized the anatomical structure for NP, DE, FG, MG, and HG (*SI Appendix,* Fig. S12*A*). The NP markers (*Aldh1a2*, *Sfrp1*, and *Sox2*) and the DE markers (*Cdh1*, *Cer1*, *Dkk1*, *Dnmt3b*, *Krt18*, *Otx2*, *Sfrp1*, and *Sox17*) were highly expressed in the brain/spinal cord and the DE regions, respectively (*SI Appendix,* Fig. S12*A*). The zoomed-in view at the boundary regions for NP and DE shows that the contact-specific genes (*Foxb1*, *Gbx2*, *Irx5*, *Lefty1*, *Pou3f1*, *Ptn*, *Sall3*, and *Socs2*) were expressed in between those two regions (*SI Appendix,* Fig. S12 *B* and *C*).

Prediction of the Neighboring Cell Type from scRNA-seq Tells the Contributing Cell Type for the Gene Expression Changes in PIC-seq. Based on the contact-specific gene expression, we originated an approach to predict neighboring cell types by using the transcriptome of single cells. The neighboring cell type can be predicted by examining specific neighbor-specific genes detected from PICs. Therefore, the contact-specific genes in the PIC-seq were used to train a multiclass SVM. The trained SVM predicts the interacting cell types of a cell by forming artificial doublets and voting from the SVM output. Among the 767 NP cells, 85 were predicted to neighbor with DE, 123 interacted with NC, and the majority (559 cells) interacted with other NP cells (Fig. 3*A*). Among the 677 DE cells, 252 were predicted to interact with NP (Fig. 3*B*). Notably, neighboring cell type prediction further informed us of the cell-type-expressing contact-specific genes. Among the contact-specific genes in the heterotypic NP+DE PICs, *Lhx5*, *Pou3f1*, *Mest*, *Ptn*, *Nkx2-1*, and *Slc1a3* were from the NP cells and *Gsc*, *Sox3*, and *Rax* were from the DE cells (Fig. 3 *A* and *B* and Dataset S5). These analyses further predicted the list of neighboring cell-specific genes expressed in each cell type. For instance, NP cells expressed *Lhx* and *Nkx2-1* when interacting with DE and *Prtg* and *Gas1* when interacting with NC cells (FDR < 0.01) (Fig. 3*A*).

To validate these contact-specific genes, we performed co-staining of FOXA2 (a DE marker), SOX2 (an NP marker), and NKX2-1 (a contact-specific gene) in the mouse embryo at E8.25. FOXA2 was expressed in DE as well as the floor plate that connects to NP. SOX2 was expressed stronger in NP (compared with DE). NKX2-1 was expressed in the part of NP cells when they were proximal to DE, consistent with our prediction (Fig. 3*C*).

We designed a specific set of experiments to experimentally validate the accuracy of the computational predictions. Focus was on a subset prediction that involves the impact of contact between the NP and DE cells on their respective transcriptome. The experimental strategy we adopted is demonstrated graphically (Fig. 4*A*). The strategy involves the isolation of NP and DE cells from E8.5 mouse embryos, using predefined cell-specific markers, NCAM-1 positive, SSEA-1 positive, and SSEA-4 negative for NP cells and CD24 positive, Claudin positive, SSEA-1 negative, and SSEA-4 negative for DE cells. The isolated cells were maintained in culture media. A specific set of DE cells were infected with comet-pD2109-CMV lentiviral particles expressing blank green fluorescent protein (GFP) and mixed with NP cells in a 1:1 ratio. The GFP-positive DE cells and GFP-negative NP cells were co-cultured for 48 h. At the end of this 48 h, the GFP-positive DE cells and GFP-negative NP cells were sorted using a flow-based cell sorter (Fig. 4*B*). The expression of 4 genes *Lhx5*, *Nkx2-1*, *Gsc,* and *Rax* was observed in the NP and DE cells maintained as a mono-culture and the NP and DE cells that were in contact with each other in a co-culture experiment (Fig. 4*C*). The qPCR-based mRNA expression analysis revealed elevated expression levels of *Lhx5* and *Nkx2-1* genes in NP cells exclusively when they were in contact with DE cells. The expression of these genes in the NP cells maintained in mono-culture was around 2.8-fold for *Lhx5* and 2.2-fold for *Nkx2-1* lower, when compared to NP cells that came in contact with DE cells. Similarly, the qPCR-based mRNA expression analysis revealed elevated expression levels of *Gsc* and *Rax* genes in DE cells exclusively when they were in contact with NP cells. The expression of these genes in the DE cells maintained in mono-culture was around 3.2-fold for *Gsc* and 3.7-fold for *Rax* lower, when compared to DE cells that came in contact with NP cells. This experiment suggests that cell–cell contact or local paracrine signaling can induce de novo gene expression at different stages of development and our computational methods are able to accurately detect these signals (Fig. 4*C*).

We also determine how long the contact-specific genes are maintained once cells are isolated. We tested the expression of genes *Lhx5*, *Nkx2-1*, *Gsc,* and *Rax* before (0 h) and after NP and DE cells were isolated with an interval of 3 h until 24 h (*SI Appendix,* Fig S13). Our results show that the expression of contact-specific genes progressively decreased to the precontact level by 9 h after separation.
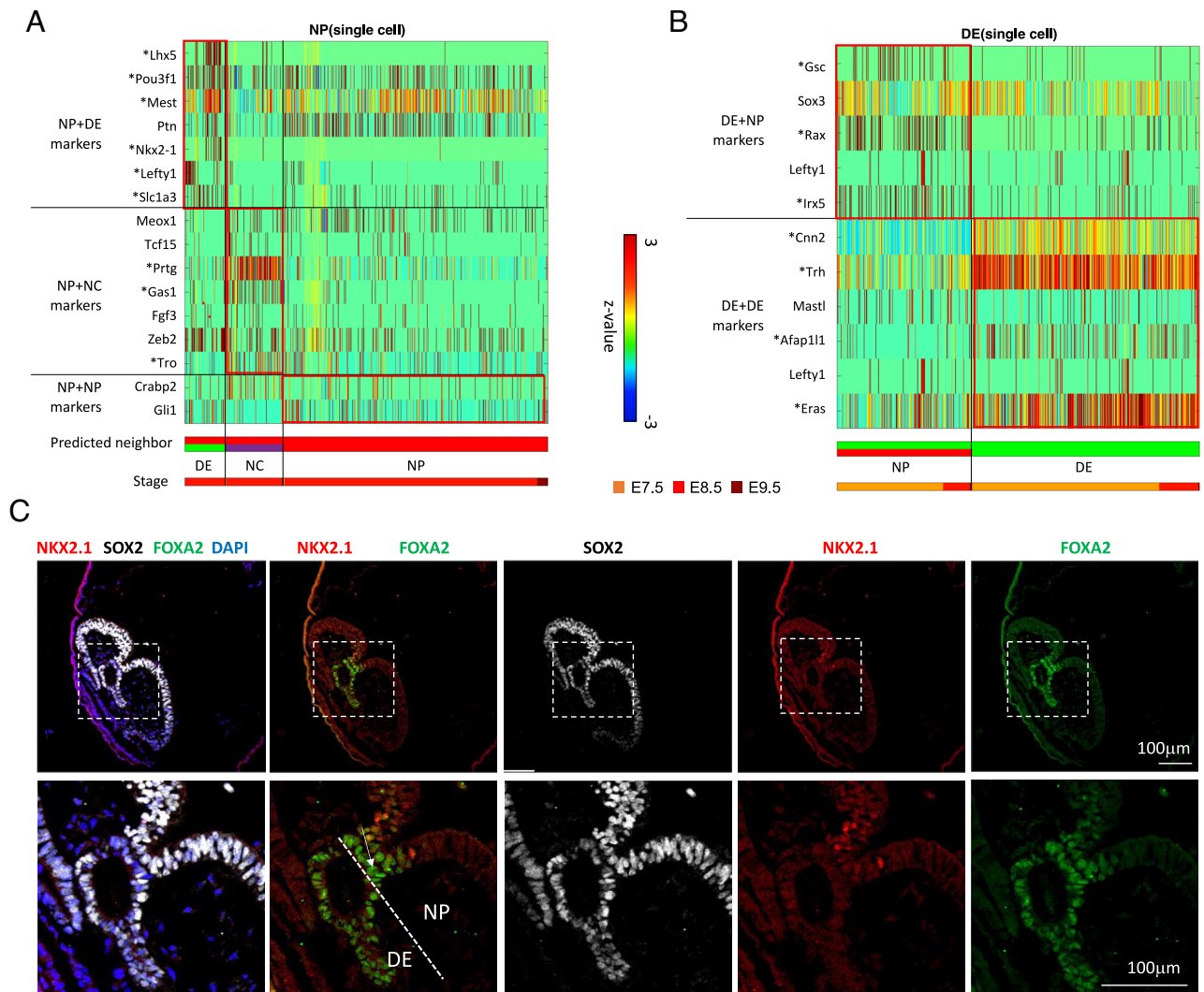
Fig. 3. Neighboring cell type prediction from scRNA-seq. (*A*) Single NP cells in the original MARS-seq dataset that are predicted to interact with DE or NC. Predictions are based on expression of defined neighbor-specific genes from PIC-seq. (*B*) Single DE cells in the original MARS-seq dataset that are predicted to interact with NP. Predictions are based on expression of defined neighbor-specific genes from PIC-seq. (*C*) Validation of a contact-specific gene Nkx2-1 using staining of a mouse embryo. Nkx2-1 is expressed in the NP (SOX2+) cells contacting with DE (FOXA2+).

We also predicted the neighboring cell type for FG, MG, HG, NC, and EmVE cells using the same strategy (*SI Appendix*, Fig. S14). We further tested if the trained SVM could annotate the neighboring cell types for publicly available scRNA-seq data from developing mouse embryos (13, 15). After the annotation, we still found the distinctive groups of DE cells expressing contact-specific genes when contacting NP such as *Rax* and *Gsc* in these independent datasets (*SI Appendix*, Figs. S15 and S16). Our results indicate that scRNA-seq retains the information about the neighboring cell type even after cells are isolated. In summary, we observed a diverse repertoire of contact-specific genes depending on their neighboring cell types.

Visualizing Spatio-Structure of Tissue Using Spatial-tSNE. Our prediction suggests that the transcriptome of a cell contains information about the neighboring cell type. However, the current visualization algorithms for scRNA-seq including UMAP (Fig. 1*B*) or t-distributed stochastic neighboring embedding (tSNE) cannot accurately represent the neighboring cell types. To visualize neighboring cells and the neighboring cell-type-specific expression profiles, we revisited the tSNE algorithm which assigns small probabilities when locating cells in the

2D plot for the cells whose transcriptomic distances are large. The spatial-tSNE algorithm we developed can visualize the neighboring cells located near each other by assigning the highest probability for the cell pairs that are classified into neighboring cells. Compared with conventional visualization approaches based on the transcriptomic similarities (Fig. 1*B*), spatial-tSNE provides information about interacting cell types in the mouse embryos. For instance, the spatial-tSNE showed the physical interactions between EmVE and DE cells (Fig. 5*A*), while they were distally located in the classical UMAP plot (Fig. 1*B*). In addition, the spatial-tSNE plot provided spatial layouts of NP+DE, MG+NC, and DE+EmVE, which are consistent with the anatomy of the mouse embryos.

The spatial-tSNE plot summarizes the neighboring cell-type-specific expression patterns in 2D embedded dimensions (Fig. 5*A*). The average expressions of NP+DE, MH+HG, and NP+NC markers were localized near the border of the corresponding two cell types (*SI Appendix*, Fig. S17). Spatial-tSNE visualizes the neighboring cell-type-specific factors. For instance, *Lhx5* is expressed in NP cells close to DE and *Gsc* is expressed more profoundly in DE cells close to NP (Fig. 5*B*).
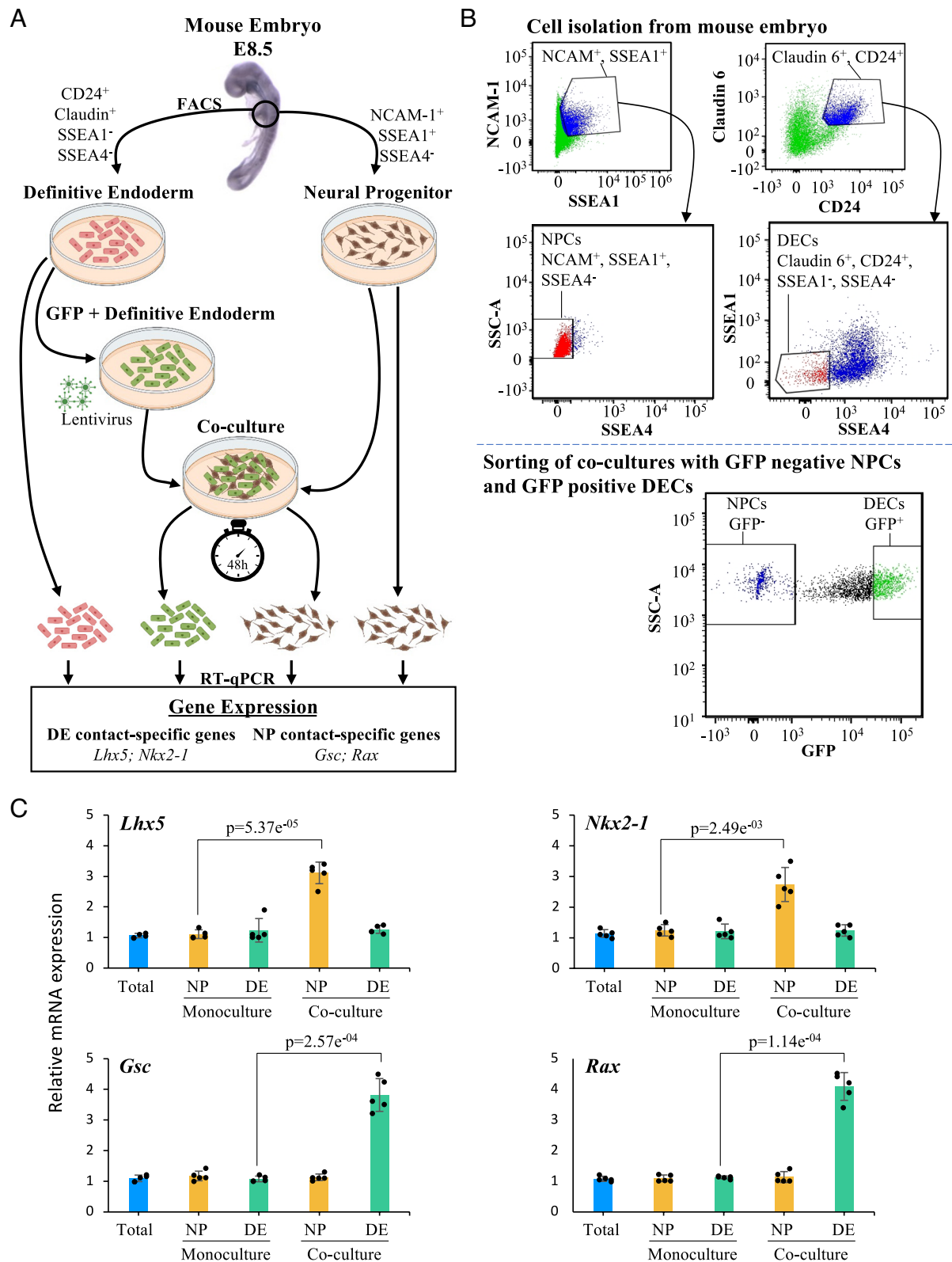
Fig. 4. Experimental validation of the neighboring cell type prediction. (*A*) A model depicting the experimental approach used to analyze changes in the expression of contact-specific genes from NP and DE cells. Briefly, we isolated NP and DE cells from E8.5 mouse embryos, tagging DE cells with GFP. Then, we performed monoculture of DE and NP cells as well as co-culture of both cell populations for 48 h. After co-culture, DE and NP cells were sorted by GFP expression. Finally, we used mono-cultured and sorted DE and NP cells to perform RT-qPCR, which allowed us to measure the expression of the DE contact-specific genes *Lhx5* and *Nkx2-1* and the NP contact-specific genes *Gsc* and *Rax*. (*B*) FACS of NP and DE cells from mouse embryo at E8.5. On the left-top gate, we sorted double-positive cells for NCAM-1 and SSEA1 (blue population). From this population we sorted SSEA4-negative cells, which represent NP cells (red population, left-middle gate). On the right-top gate, we sorted double-positive cells for Claudin-6 and CD24 (blue population). Then, we sorted SSEA1- and SSEA4-negative cells, to obtain DE cells (red population, right-middle gate). The bottom gate shows the sorting of DE and NP cells after co-culture for 48 h. Cells were sorted accordingly to GFP expression since DE cells were tagged with GFP prior to their use in the co-culture experiment. (*C*) The analysis through RT-qPCR of contact-specific genes from NP and DE cells shows that after co-culture, NP cells upregulate *Lhx5* ($P = 5.37E−5$) and *Nkx2-1* ($P = 2.49E−3$) while DE cells increase the expression of *Gsc* ($P = 2.57E−4$) and *Rax* ($P = 1.14E−4$). Expression in these genes in the total embryonic tissue represents the control (lane 1, blue bar in every plot); the relative expression of these genes in the monoculture and coculture is calculated relative to the expression of these genes in the total embryonic tissue (N = 5). We performed a two-tailed Student's *t* test.
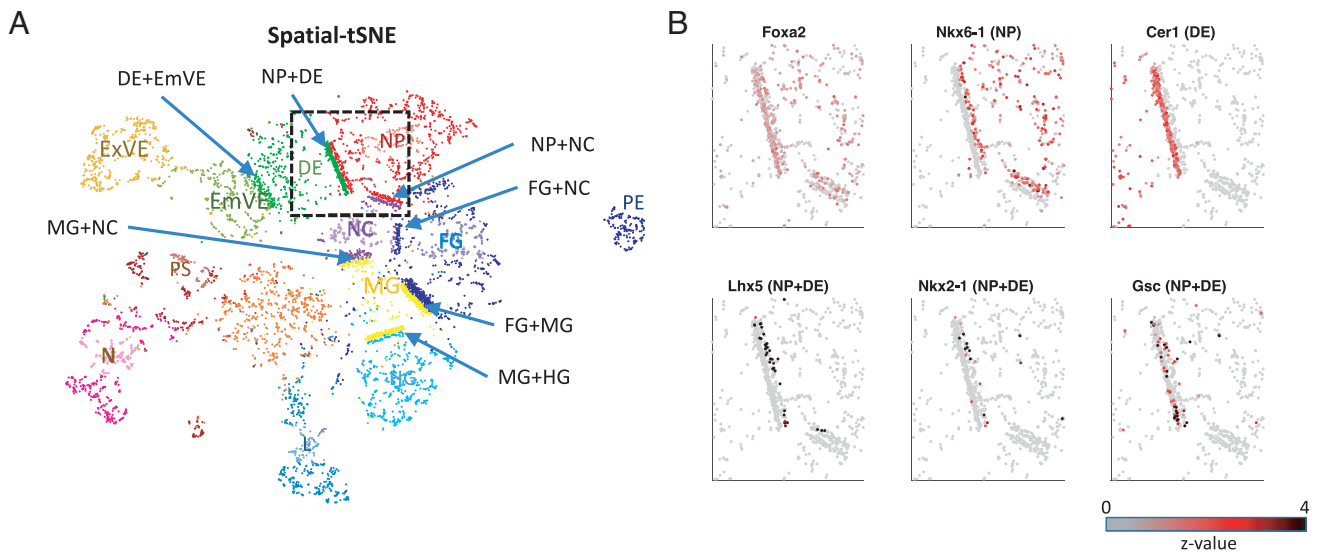
Fig. 5. Visualizing spatio-structure of tissue using spatial-tSNE for scRNA-seq. (*A*) A spatial-tSNE plot recapitulating the spatial distribution of cells in mouse embryos. (*B*) Expression patterns of NP, DE, and NP+DE markers on the spatial-tSNE plot for the boxed region in *A*.

Discussion

Cells are influenced by the neighboring cells in many ways, including cell size, stiffness, and mechanical forces (44, 45). During embryogenesis, coordination between adjacent cells is essential to regulate the expression of genes in correct spatial and temporal contexts. To establish these patterns during morphogenesis, these cells influence each other's gene expression by exploiting various signaling molecules, direct cell–cell contact (46), or reconfiguring the mechanical environment (47, 48).

Here, we asked if there are unique genes expressed when cells are in contact with each other. To obtain cell–cell contact information, we used PIC-seq and established computational algorithms to identify neighboring cell-type-specific gene expression. PIC-seq, by retaining cell contact, enabled us to predict neighboring cell-type-specific gene expression. Our predictions indicated that cells present specific gene expression patterns depending on their neighboring cell type (Fig. 3*A*). For instance, NP cells expressed *Lhx5* and *Nkx2-1* when neighboring DE and *Gas1* when neighboring with more posterior NC.

To confirm our observation in an unbiased way, we used independent publicly available Geo-seq (24) and seqFISH (43) datasets. The neighbor-specific genes we identified were spatially expressed between the regions marked for each cell type (Fig. 2). Even though Geo-seq (24) is limited to the mouse embryos at E7.5, it was sufficient to highlight the likely spatial location of pairs of interactors for NP+DE, ExVE+EmVE, and NP+NC (*SI Appendix*, Fig. S10). The seqFISH data (43) also confirmed that neighbor-specific genes are expressed in the regions between two cell types.

We further questioned if cell contact or proximity induces specific gene expression. For this, we devised a co-culture system followed by sorting individual cell types and measured gene expression changes (Fig. 4). Our experimental strategy clearly showed that there are genes induced by cell contact or proximity, and PIC-seq provided an approach to obtain this information in an unbiased manner.

Among the predicted neighboring cell-type-specific genes, we identified several factors with established roles during development. For instance, *Lhx5*, a gene expressed in NP cells when contacting DE, is known to promote forebrain development by

regulating the Wnt signaling pathway (33). Knockdown of *Lhx5* resulted in apoptotic hypothalamic development (49). *Nkx2-1*, another gene expressed in NP cells when contacting DE, is also recognized for its role in response to dorsal–ventral patterning in the neural tube and for specifying cortical interneuron subtypes (34). Also, DE cells interacting with NP cells expressed *Gsc* (Figs. 2*A* and 3*B*) which has a role in EA (35), prechordal plate (36), DE differentiation (38), and FG formation (39). Our results indicate that cell contact or proximity has the potential to activate cell type specification during embryogenesis.

Our study indicates that a cell encodes details about its local environment in its transcriptome. For instance, single NP cells identified as interacting with DE retained the expression of *Nkx2-1* even after cell isolation (Figs. 2*A* and 3*A*). Based on the local information detailed in the transcriptome of a cell, we were able to predict its neighboring cell type (Fig. 3 *A* and *B*). The trained model was further applied to identifying neighboring cell types for publicly available scRNA-seq during embryogenesis (13, 15) (*SI Appendix*, Figs. S13 and S14). This indicates that the contact-specific genes identified from PIC-seq can be used as a reference to reannotate the neighboring cell types of public scRNA-seq.

Gene expression varied between cells as a function of their neighbors. In our study, NP cells interacting with DE cells expressed *Lhx5* and *Nkx2-1*, and those interacting with NC expressed *Prtg* (Fig. 3*A*). These findings may underlie anterior–posterior axis inducing activities of these N derivatives. The EA emerges very early in gastrulation to pattern the presumptive anterior neural plate, while the NC emerges later, patterning more posterior locations along the neural tube. Deconstructing positional information within the transcriptome could provide a detailed map of cells localized to the axis promoting organizing centers that emerge in embryonic development. Given the role of the EA in patterning the nascent neural plate (10) and NC for the patterning of the neural tube (50–52), our identification of NP+DE and NP+NC supports the inductive profile of these cells.

A widely used approach to understand cell communication is to use ligand–receptor pairs (16, 17). We did not find the overlap between the genes identified by a ligand–receptor analysis using CellPhoneDB (17) and the contact-specific genes identified by PIC-seq (*SI Appendix*, Fig. S18). Moreover, the cell types predicted to

be communicating frequently using ligand–receptor pairs do not reflect well with the anatomical structure (*SI Appendix*, Fig. S19). These observations indicate that PIC-seq enabled the investigation of cell contact-associated gene expression which cannot be studied using ligand–receptor pairs. Furthermore, the use of co-expression of ligand–receptor pairs only shows the most frequently interacting cells and does not explain specific cells engaged in cell-cell communication. The cell contact information derived from PIC-seq may provide additional layers of detail, explicitly unravelling inductive cell interactions.

We developed spatial-tSNE to visualize the spatial proximity that we predicted. Previous visualization methods locate cells mainly based on transcriptomic similarities. The UMAP plot using scRNA-seq data appears to reflect the spatial organization of EmVE and ExVE as well as FG, MG, and HG, because their gene expression similarities reflect their spatial interactions (Fig. 1*B*). However, transcriptome-based visualization could not represent the physical interaction of NP+DE, MG+NC, and NP+EmVE, while these are well visualized in the spatial-tSNE (Fig. 5*A*). Consistent with this representation, contact-specific genes are found in association with their locations in the spatial-tSNE plot (Fig. 5*B*). Spatial-tSNE depends on the prediction of neighboring cell types (Fig. 3 *A* and *B* and *SI Appendix*, Fig. S12). In this work, we used 367 PICs for training. The performance of neighboring cell type prediction can be further improved as we accumulate more PICs for training. Even though spatial-tSNE cannot represent the real 3D structure of a tissue, it provides a more comprehensive map for context-dependent relationships inherent in mammalian development. In addition, the computational approaches that we designed for PIC-seq can also be applied to image-based spatial transcriptomics data, such as seqFISH (43), to identify contact-specific and regulated genes.

As our study is about de novo gene discovery, it is difficult to assign specific roles in mechanobiology, although *Gsc* is a known marker of the N (53), a region that has inductive properties in heterotopic grafting experiments (54). The history of developmental biology is based on a large number of embryonic grafting experiments to define inductive interactions that occur during development (12). Grafting experiments were pivotal in our understanding of how signals produced from one cell can illicit patterning responses in another cell. However, grafting experiments are technically challenging and inherently limited to a predefined set of interactions. Here, we take an unbiased approach to understand developmental context, producing spatial-tSNEs to provide an unbiased catalog of potential developmental interactions. Through assessing these interactions, one could develop a comprehensive map of embryonic induction providing a set of all possible sites. While directionality can only be inferred by experiments, we present an impartial approach to study spatial gene regulation during development.

STAR Methods

Multiplet Cell Isolation. Mouse FOXA2[Venus] embryos were collected between embryonic days (E) 7.5 and 9.5. The E9.5 embryos were dissected in order to enrich the sample with gut endoderm cells. Embryos were dissociated with Accutase (Sigma) into multiplet cells immediately after collection. The collected embryos were mixed with mouse ESC, which were counterstained with CellVue Maroon Cell Labeling Kit (Thermofisher, # 88-0870-16) to increase the number of cells in the sample in order to avoid loss of the scarce FOXA2[Venus]-positive cells by spinning. The samples were then incubated with prewarmed Accutase at 37 °C. For the multiplet cell dissociation, the samples were incubated for 4 min with 1 mL Accutase and pipetted up and down carefully to ensure that cells were not dissociated into single cells. The Accutase was diluted by adding 3ml of FACS buffer 1 (10% FBS in PBS) and spun down. The cells were washed with FACS buffer 1 two more times and transferred to a FACS tube with FACS-DAPI buffer for the FACS process.

Flow Cytometry and Multiplet Cell Capturing. Multiplet cells were isolated from FOXA2[Venus] mouse embryos. Cells were sorted using a BD FACS Aria III. FSC/SSC gates were used to define a homogeneous population, FSC-H/FSC-W gates were used to include multiplets and remove singlets, and dead cells were excluded based on DAPI inclusion. The sorting speed was kept at 100 to 300 events/s to eliminate sorting two or more drops containing cells into one well. Single-drop deposition into the 384-well plates was verified colorimetrically based on a previously published protocol (55). Cells were sorted directly into the lysis buffer containing first RT primer and RNase inhibitor, immediately frozen, and later processed by MARS-seq protocol as described previously (27).

Flow Cytometry and Cell Sorting of NP and DE Populations. Embryonic cells were isolated from E8.5 mouse embryos and incubated with cell surface antibodies specific to NP and DE cell populations. Following the incubation, these populations were sorted using BD FACSAria Fusion, and data were analyzed by FACSDiva 8.0.2 software as follows. FSC/SSC gates were used to define a homogeneous population, and FSC-H/FSC-A gates were used to sort singlets exclusively. For the purpose of isolating the NP cells, the embryonic cells were suspended in FACS buffer 2 (PBS, 1mM EDTA, 25mM HEPES pH 7, 2% FBS) and stained with NCAM-1:PE (Biolegend #125618), SSEA1:APC (Abcam #ab18277), and SSEA4:Alexa Fluor 488 (Thermo Fisher Scientific # 53-8843-42). The NCAM-1 (56)/SSEA1 (57) gate was used to select double-positive populations, from which SSEA4-negative cells were selected using the SSC/SSEA4 gate as described previously (57).

For the purpose of isolating the DE cells, the embryonic cells were suspended in FACS buffer 2 and stained with SSEA1:APC, SSEA4:PE (Thermo Fisher Scientific # 12-8843-42), Claudin-6:FITC (Bioss #bs-3754R-FITC), and CD24:BV421 (BD Horizon™ #562563). Here, the CD24 (58)/Claudin-6 (59) gate was used to select double-positive cells followed by the selection of populations negative for SSEA1 and SSEA4 using the SSEA1/SSEA4 gate to avoid contamination with NP and visceral endoderm cells (57, 58). Isolated NP and DE cells were maintained in culture using the StemFlex Medium (Thermo Fisher) at 37 °C, 5% CO2 incubator.

A subpopulation of the DE cells were infected with 10^9 TU/ml of GFP comet-pD2109-CMV lentiviral particles (ATUM) and 5 μg/ml of polybrene. After 24h infection, GFP-positive DE cells were selected by GFP expression using BD FACSAria. Following a 48-h co-culture of GFP+ DE and GFP- NP cells in a 1:1 ratio, the BD FACSAria was used to sort the GFP-positive DE cells and GFP-negative NP cells according to their GFP expression using SSC/GFP gate.

DE and NP Contact-Specific Genes Quantification by RT-qPCR. We isolated total RNA from DE and NP cells individual cultures and cocultures using the PureLink RNA Mini kit, as per the manufacturer's instruction, and eluted total RNA in 50 μL RNase/DNase-free H_2O. Then, we reverse-transcribed to cDNA 10 ng of total RNA using Superscript Vilo cDNA synthesis kit. Finally, we performed real-time PCR (qPCR) in QuantStudioTM

5 (Applied Biosystems) using PowerUp SYBR Green master mix (Thermo Fisher Scientific) and the following reaction conditions. The initial denaturation step was performed at 95 °C for 2 min, followed by 40 cycles of 95 °C for 15 s and 60 °C for 60 s. We used the comparative CT method ($\Delta\Delta$Ct) to quantify relative gene expression, normalizing the expression of our target genes with the housekeeping gene *Gapdh*. All samples were run using the following primers: *Gapdh*: 5′-CATCACTGCCACCCAGAAGACTG-3′ (F) and 5′-ATGCCAGTGAGCTTCCCGTTCAG-3′ (R); *Lhx5*: 5′-CTCGACCGCTTTCTGCTGAA-3′ (F) and 5′-CGCTCG-GAGAGATACCTTGC-3′ (R); *Nkx2-1*: 5′-AGGACACCAT GCGGAACAG-3′ (F) and 5′- CCATGCCGCTCATATTCA TGC-3′ (R); *Gsc*: 5′-GACGAAGTACCCAGACGTGG-3′ (F) and 5′-CGGTTCTTAAACCAGACCTCCA-3′ (R); and *Rax*: 5′-TGGGCTTTACCAAGGAAGACG-3′ (F) and 5′-GGTAG-CAGGGCCTAGTAGCTT-3′ (R).

Data Processing of scRNAseq and PIC-seq Data of Mouse Embryo. All scRNA-seq libraries were sequenced using Illumina NextSeq 500. Sequences were mapped to mouse mm9 genome, demultiplexed, and filtered as previously described (27, 28). We estimated the level of spurious unique molecular identifiers (UMIs) in the data using statistics on empty MARS-seq wells as previously described (27). Mapping of reads was done using HISAT (version 0.1.6) (60); reads with multiple mapping positions were excluded.

Among the transcriptome of 6,600 single cells and 382 PICs, we filtered the low-quality samples that had UMI counts over 2^{17} or less than 256 2^8. The remaining samples contained 6,288 single cells and 367 PICs. To remove any batch effect, we used the Seurat v3 standard integration workflow (61). The 13 clusters were obtained using a graph-based Louvain clustering algorithm.

SVMs for Classification. For the classification of PICs, we trained a multiclass classifier for SVMs using a MATLAB (version R2020a) function 'fitcecoc'. The classifier consists of multiple SVM binary learners in a one-vs.-one design. We trained three SVMs for each stage (E7.5, E8.5, and E9.5) of PIC-seq and scRNAseq data. We used the major clusters for each stage (DE, N, ExVE, EmVE, PS, and PE for E7.5; NP, FG, DE, MG, HG, and NC for E8.5; and FG, MG, HG, L, and NC for E9.5) and the top 5 DEGs for each cluster. We run 10-fold cross-validation for the trained models using a MATLAB function 'crossval' and calculated the error rate using 'kFoldLoss' with 10. We calculated the significance of the frequencies of PICs against doublets identified from scRNAseq using Fisher's exact test.

SVMs for Neighboring Cell Type Prediction. For the prediction of the identity of neighboring cells, we applied multiclass SVM using fitcecoc function in MATLAB R2020a. We only used the contact-specific genes for training and prediction. The SVMs for each cell type were trained using the PIC-seq data with their annotations. For example, to train an SVM for NP, PICs included in NP+NP, NP+DE, and NP+NC were used. To predict the neighboring cell type from the single-cell transcriptome, we made artificial PIC-seq by mixing the transcriptome of the cell of interest with all other cells one by one. The artificial PIC-seq data for the cell of interest were predicted using the corresponding SVM. The voting scheme (i.e., most frequent) is used to assign the neighboring cell type. We applied this scheme to all single cells.

Statistical Analysis and Enrichment Analysis. The *P* value for cell-type-specific and contact-specific marker genes was calculated by using a two-sided Wilcoxon rank sum test. The *P* value for RT-qPCR of contact-specific genes was calculated by using a two-sided Student's *t* test. We used Enrichr (40), an enrichment analysis tool, to investigate the enriched GO terms and KEGG pathways for each marker gene group.

Staining of Mouse Embryo. E8.5 embryos were isolated in PBS and then fixed overnight in 4% paraformaldehyde (PFA) overnight at 4 °C. The following day, embryos were washed in PBT (PBS containing 0.1% Tween-20), dehydrated in an ascending methanol sequence, xylene treated, embedded in paraffin, and sectioned at 6.5 μm. Immunofluorescence was performed on 6.5-μm deparaffinized sections. The sections were subjected to antigen retrieval in Tris buffer pH 10.2 for 10 min, washed in 0.1% PBT, and incubated in blocking buffer (0.5% milk powder, 99.5% PBT) for 2 h at room temperature. Primary antibodies were incubated in a blocking buffer overnight at f4 °C. The following day, the sections were washed three times with PBT and incubated for 1 h with corresponding secondary antibodies in a blocking buffer at room temperature. After three washes in PBT, DAPI (Sigma-Aldrich, 1:2,000) was added to counter-stain the nuclei. The sections were mounted using Prolong Gold Antifade Reagent (Invitrogen, P36934) and imaged using Zeiss LSM-700 confocal microscope. The following primary antibodies were used: FOXA2 (Thermofisher, 7H4B7, 1:250), SOX2 (eBioscience, 14-9811-80, 1:250), and NKX2-1 (Abcam, ab76013, 1:250). Secondary antibodies were Alexa Fluor conjugates 488, 555, and 647 (Life Technologies) at 1:500.

Spatial-tSNE. Spatial-tSNE is designed for visualization of neighboring cells in scRNA-seq data, which is modified from tSNE (62) by considering neighboring cell information. In the original tSNE, the 2D embeddings are obtained by rearranging each cell based on the probability of the pairwise similarities of the cells on the original high-dimensional space. The pairwise similarity of two cells i and j in the high-dimensional space is defined by the probability, $p_{ij} = \frac{\exp\left(-\|x_i - x_j\|^2 / 2\sigma_i^2\right)}{\sum_{k \neq i}\exp\left(-\|x_i - x_k\|^2 / 2\sigma_i^2\right)}$, where x_i is the data points of cell i and σ_i is the variance of the Gaussian which is centered on data point x_i. The distance between two cells in the reduced t-SNE dimension is determined by the probability p_{ij} in high-dimensional space.

Spatial-tSNE shows the clustering and spatial information at the same time by changing the similarity probability for the cells that are predicted to neighbor with each other. To reflect spatial information in the t-SNE dimension, we modified the probability p_{ij} so that the similarity probability of two neighboring cells is the maximum probability of all pairs. With these modified probabilities, the predicted neighbor cells are located at the border of the two clusters without ruining the relative position of other cells. To clearly visualize neighbored cells, an imaginary line was drawn between the two populations, which can be rotated so that cells have the longest distance to it. Other cells are rearranged based on their probabilities.

Author affiliations: [a]Biotech Research and Innovation Centre, University of Copenhagen, Copenhagen N 2200, Denmark; [b]School of Systems Biomedical Science, Soongsil University, Dongjak-Gu, Seoul 06978, Republic of Korea; [c]Novo Nordisk Foundation Center for Stem Cell Medicine (reNEW), University of Copenhagen, Copenhagen 2200, Denmark; [d]Champalimaud Centre for the Unknown, Lisbon 1400-038, Portugal; [e]Department of Biology, Stanford University, Stanford, CA 94305; [f]Department of Immunology, Weizmann Institute of Science, Rehovot 7610001, Israel; [g]Department of Surgery, Virginia Commonwealth University, Richmond, VA 23298-0033; [h]School of Medicine, Virginia Commonwealth University Massey Cancer Center, Virginia Commonwealth University, Richmond, VA 23298-0033; [i]Department of Human and Molecular Genetics, School of Medicine, Virginia Commonwealth University, Richmond, VA 23298-0033; [j]School of Medicine, VCU Institute of Molecular Medicine, Virginia Commonwealth University, Richmond, VA 23298-0033; and [k]Department of Computational Biomedicine, Cedars-Sinai Medical Center, Los Angeles, CA 90069

Author contributions: R.G., J.M.B., and K.J.W. designed research; J.K., M.M.R., E.M., S.R., G.W., A.M.P., E.D., A.G.-G., P.B.F., R.G., and K.J.W. performed research; J.K., M.M.R., E.M., S.R., A.M.P., L.L., I.A., M.C.H., J.M.B., R.G., and K.J.W. analyzed data; and J.K., M.M.R., E.M., A.M.P., V.V., E.M., R.W., J.T., P.B.F., J.M.B., R.G., and K.J.W. wrote the paper.

1. S. G. Babb, J. A. Marrs, E-cadherin regulates cell movements and tissue formation in early zebrafish embryos. *Dev. Dyn.* **230**, 263–277 (2004).
2. B. Goldstein, Induction of gut in Caenorhabditis elegans embryos. *Nature* **357**, 255–257 (1992).
3. N. Guisoni, R. Martinez-Corral, J. Garcia-Ojalvo, J. de Navascues, Diversity of fate outcomes in cell pairs under lateral inhibition. *Development* **144**, 1177–1186 (2017).
4. L. Larue *et al.*, A role for cadherins in tissue formation. *Development* **122**, 3185–3194 (1996).
5. M. Michel, I. Raabe, A. P. Kupinski, R. Perez-Palencia, C. Bokel, Local BMP receptor activation at adherens junctions in the Drosophila germline stem cell niche. *Nat. Commun.* **2**, 415 (2011).
6. O. Shaya *et al.*, Cell-cell contact area affects notch signaling and notch-dependent patterning. *Dev. Cell* **40**, 505–511.e506 (2017).
7. R. O. Stephenson, Y. Yamanaka, J. Rossant, Disorganized epithelial polarity and excess trophectoderm cell fate in preimplantation embryos lacking E-cadherin. *Development* **137**, 3383–3391 (2010).
8. O. Tassy, F. Daian, C. Hudson, V. Bertrand, P. Lemaire, A quantitative approach to the study of cell shapes and interactions during early chordate embryogenesis. *Curr. Biol.* **16**, 345–358 (2006).
9. M. D. Yoder, B. M. Gumbiner, Axial protocadherin (AXPC) regulates cell fate during notochordal morphogenesis. *Dev. Dyn.* **240**, 2495–2504 (2011).
10. P. Thomas, R. Beddington, Anterior primitive endoderm may be responsible for patterning the anterior neural plate in the mouse embryo. *Curr. Biol.* **6**, 1487–1496 (1996).
11. H. Spemann, H. Mangold, Induction of embryonic primordia by implantation of organizers from a different species. 1923. *Int. J. Dev. Biol.* **45**, 13–38 (2001).
12. G. E. Solini, C. Dong, M. Saha, Embryonic transplantation experiments: Past, present, and future. *Trends Dev. Biol.* **10**, 13–30 (2017).
13. S. Nowotschin *et al.*, The emergent landscape of the mouse gut endoderm at single-cell resolution. *Nature* **569**, 361–367 (2019).
14. J. Cao *et al.*, The single-cell transcriptional landscape of mammalian organogenesis. *Nature* **566**, 496–502 (2019).
15. B. Pijuan-Sala *et al.*, A single-cell molecular map of mouse gastrulation and early organogenesis. *Nature* **566**, 490–495 (2019).
16. R. Vento-Tormo *et al.*, Single-cell reconstruction of the early maternal-fetal interface in humans. *Nature* **563**, 347–353 (2018).
17. M. Efremova, M. Vento-Tormo, S. A. Teichmann, R. Vento-Tormo, Cell PhoneDB: Inferring cell-cell communication from combined expression of multi-subunit ligand-receptor complexes. *Nat. Protoc.* **15**, 1484–1506 (2020).
18. J. C. Herve, M. Derangeon, Gap-junction-mediated cell-to-cell communication. *Cell Tissue Res.* **352**, 21–31 (2013).
19. J. C. Boisset *et al.*, Mapping the physical network of cellular interactions. *Nat. Methods* **15**, 547–553 (2018).
20. K. B. Halpern *et al.*, Paired-cell sequencing enables spatial gene expression mapping of liver endothelial cells. *Nat. Biotechnol.* **36**, 962–970 (2018).
21. B. M. Szczerba *et al.*, Neutrophils escort circulating tumour cells to enable cell cycle progression. *Nature* **566**, 553–557 (2019).
22. A. Giladi *et al.*, Dissecting cellular crosstalk by sequencing physically interacting cells. *Nat. Biotechnol.* **38**, 629–637 (2020).
23. N. Andrews *et al.*, An unsupervised method for physical cell interaction profiling of complex tissues. *Nat. Methods* **18**, 912–920 (2021).
24. G. Peng *et al.*, Molecular architecture of lineage allocation and tissue organization in early mouse embryo. *Nature* **572**, 528–532 (2019).
25. I. Burtscher, W. Barkey, H. Lickert, Foxa2-venus fusion reporter mouse line allows live-cell analysis of endoderm-derived organ formation. *Genesis* **51**, 596–604 (2013).
26. M. M. Rothova *et al.*, Identification of the central intermediate in the extra-embryonic to embryonic endoderm transition through single-cell transcriptomics. *Nat. Cell Biol.* **24**, 833–844 (2022).
27. D. A. Jaitin *et al.*, Massively parallel single-cell RNA-seq for marker-free decomposition of tissues into cell types. *Science* **343**, 776–779 (2014).
28. H. Keren-Shaul *et al.*, MARS-seq2.0: An experimental and analytical pipeline for indexed sorting combined with single-cell RNA sequencing. *Nat. Protoc.* **14**, 1841–1862 (2019).
29. H. L. Byun, S. W. Lee, A survey on pattern recognition applications of support vector machines. *Int. J. Pattern Recognit. Artif. Intelligence* **17**, 459–486 (2003).
30. C. S. McGinnis, L. M. Murrow, Z. J. Gartner, DoubletFinder: Doublet detection in single-cell RNA sequencing data using artificial nearest neighbors. *Cell Syst.* **8**, 329–337 e324 (2019).
31. G. S. Kwon, M. Viotti, A. K. Hadjantonakis, The endoderm of the mouse embryo arises by dynamic widespread intercalation of embryonic and extraembryonic lineages. *Dev. Cell* **15**, 509–520 (2008).
32. S. L. Lewis, P. P. Tam, Definitive endoderm of the mouse embryo: Formation, cell fates, and morphogenetic function. *Dev. Dyn.* **235**, 2315–2329 (2006).
33. G. Peng, M. Westerfield, Lhx5 promotes forebrain development and activates transcription of secreted Wnt antagonists. *Development* **133**, 3191–3200 (2006).
34. S. J. Butt *et al.*, The requirement of Nkx2-1 in the temporal specification of cortical interneuron subtypes. *Neuron* **59**, 722–732 (2008).
35. J. A. Belo *et al.*, Cerberus-like is a secreted factor with neutralizing activity expressed in the anterior primitive endoderm of the mouse gastrula. *Mech. Dev.* **68**, 45–57 (1997).
36. E. Hermesz, S. Mackem, K. A. Mahon, Rpx: A novel anterior-restricted homeobox gene progressively activated in the prechordal plate, anterior neural plate and Rathke's pouch of the mouse embryo. *Development* **122**, 41–52 (1996).
37. J. K. Earls, J. Sin, K. Ye, Mechanobiology of human pluripotent stem cells. *Tissue Eng. Part B. Rev.* **19**, 420–430 (2013).
38. K. Daneshvar *et al.*, DIGIT is a conserved long noncoding RNA that regulates GSC expression to control definitive endoderm differentiation of embryonic stem cells. *Cell Rep.* **17**, 353–365 (2016).
39. M. Hansson *et al.*, A late requirement for Wnt and FGF signaling during activin-induced formation of foregut endoderm from mouse embryonic stem cells. *Dev. Biol.* **330**, 286–304 (2009).
40. M. V. Kuleshov *et al.*, Enrichr: A comprehensive gene set enrichment analysis web server 2016 update. *Nucleic. Acids. Res.* **44**, W90–97 (2016).
41. Y. Liu *et al.*, Sox17 is essential for the specification of cardiac mesoderm in embryonic stem cells. *Proc. Natl. Acad. Sci. U.S.A.* **104**, 3859–3864 (2007).
42. J. Lu, J. Qian, D. Keppler, W. V. Cardoso, Cathepsin H is an Fgf10 target involved in Bmp4 degradation during lung branching morphogenesis. *J. Biol. Chem.* **282**, 22176–22184 (2007).
43. T. Lohoff *et al.*, Integration of spatial and single-cell transcriptomic data elucidates mouse organogenesis. *Nat. Biotechnol.* **40**, 74–85 (2022).
44. V. Barone *et al.*, An effective feedback loop between cell-cell contact duration and morphogen signaling determines cell fate. *Dev. Cell* **43**, 198–211. e112 (2017).
45. E. Hannezo, C. P. Heisenberg, Mechanochemical feedback loops in development and disease. *Cell* **178**, 12–25 (2019).
46. N. Perrimon, C. Pitsouli, B. Z. Shilo, Signaling mechanisms controlling cell fate and embryonic patterning. *Cold Spring Harb. Perspect. Biol.* **4**, a005975 (2012).
47. C. P. Heisenberg, Y. Bellaiche, Forces in tissue morphogenesis and patterning. *Cell* **153**, 948–962 (2013).
48. N. I. Petridou, S. Grigolon, G. Salbreux, E. Hannezo, C. P. Heisenberg, Fluidization-mediated tissue spreading by mitotic cell rounding and non-canonical Wnt signalling. *Nat. Cell Biol.* **21**, 169–178 (2019).
49. A. Miquelajauregui *et al.*, LIM homeobox protein 5 (Lhx5) is essential for mamillary body development. *Front. Neuroanat.* **9**, 136 (2015).
50. O. Cleaver, P. A. Krieg, Notochord patterning of the endoderm. *Dev Biol* **234**, 1–12 (2001).
51. S. Balmer, S. Nowotschin, A. K. Hadjantonakis, Notochord morphogenesis in mice: Current understanding & open questions. *Dev. Dyn.* **245**, 547–557 (2016).
52. F. Barrionuevo, M. M. Taketo, G. Scherer, A. Kispert, Sox9 is required for notochord maintenance in mice. *Dev. Biol.* **295**, 128–140 (2006).
53. M. Blum *et al.*, Gastrulation in the mouse:the role of the homeobox gene goosecoid. *Cell* **69**, 1097-1106 (1992).
54. R. S. Beddington, Induction of a second neural axis by the mouse node. *Development* **120**, 613–620 (1994).
55. O. R. Rodrigues, S. Monard, A rapid method to verify single-cell deposition setup for cell sorters. *Cytometry A* **89**, 594–600 (2016).
56. W. F. Bai *et al.*, Isolation and characterization of neural progenitor cells from bone marrow in cell replacement therapy of brain injury. *Front. Cell Neurosci.* **14**, 49 (2020).
57. P. Noisa *et al.*, Identification and characterisation of the early differentiating cells in neural differentiation of human embryonic stem cells. *PLoS One* **7**, e37129 (2012).
58. R. I. Sherwood *et al.*, Prospective isolation and global gene expression analysis of definitive and visceral endoderm. *Dev. Biol.* **304**, 541–555 (2007).
59. W. J. Anderson *et al.*, Genetic targeting of the endoderm with claudin-6CreER. *Dev. Dyn.* **237**, 504–512 (2008).
60. D. Kim, B. Langmead, S. L. Salzberg, HISAT: A fast spliced aligner with low memory requirements. *Nat. Methods* **12**, 357–360 (2015).
61. T. Stuart *et al.*, Comprehensive integration of single-cell data. *Cell* **177**, 1888–1902.e1821 (2019).
62. L. H. van der Maaten, G. Hinton, Visualizing data using t-SNE. *J. Mach. Learn. Res.* **9**, 2579–2605 (2008).
63. J. Kim, M. M. Rothova, D. Eyal, Physically interacting cell sequencing of mouse embryonic endoderm at E7.5, E8.5, and E9.5. Gene Expression Omnibus(GEO). https://www.ncbi.nlm.nih.gov/geo/query/acc.cgi?acc=GSE182393. Deposited 3 August 2022.